Stability of Polarons and Oxygen Vacancies in $BiVO_4$ Revealed by Machine-Learning-Driven Simulations

Ethan Berger,* Tobias Hainer, Tobias Möslinger, Paul Erhart, and Julia Wiktor†

Department of Physics and Astronomy, Chalmers University of Technology, SE-41296 Gothenburg, Sweden

(Received 2 April 2026; revised 20 May 2026; accepted 17 June 2026; published 9 July 2026)

Bismuth vanadate is a promising photoanode material for photoelectrocatalytic water splitting. Localized charges play a crucial role in the water-splitting mechanism by introducing charge-transition levels within the band gap and thereby modifying the band alignment. Additionally, the introduction of oxygen vacancies, which can interact with electron polarons, has been reported to improve the photoelectrocatalytic efficiency. However, charge-transition levels are typically evaluated at 0 K, whereas operating conditions involve finite temperatures and, in thin films, epitaxial strain. Capturing these effects requires free energies and extensive sampling that are generally prohibitive for *ab initio* methods. In this work, we train a machine-learned interatomic potential for $BiVO_4$, including electron polarons and oxygen vacancies in various charge states, to resolve how free energies, transition levels, and charge trapping evolve under operando temperature and strain conditions. For oxygen vacancies, the use of a machine-learned potential enables efficient sampling of charge-localization sites in the vicinity of the vacancy, revealing favored configurations. The energies of the localized polaron and oxygen-vacancy states remain essentially unchanged with temperature, while their transition levels relative to the band edges vary due to temperature-dependent band-edge shifts. In contrast, strain more strongly modifies both the localized states and the band edges. These results provide new insights into the stability of localized charges and their role in photoelectrocatalytic water splitting at finite temperature.

DOI: 10.1103/xwxv-6s55

I. INTRODUCTION

Photoelectrocatalytic (PEC) water splitting is a clean method for producing hydrogen from water and solar energy [1–3]. PEC relies on the hydrogen evolution reaction (HER) at the cathode and the oxygen evolution reaction (OER) at the anode [2,4]. In an efficient setup, the conduction band minimum (CBM) of the cathode must lie above the HER, while the valence band maximum (VBM) of the anode must lie below the OER. This requirement implies that photoexcited charges occupy delocalized band states. However, in semiconductors, charges can localize due to doping [5], point defects [6,7], or polaron formation [8,9], resulting in additional energy levels within the band gap. These charge-transition levels (CTLs) affect PEC efficiency by either improving or degrading band alignment with HER and OER. Thorough investigations of these additional energy levels are therefore crucial to identify potential candidates for PEC applications.

Transition metal oxides have been suggested as photoanodes for PEC water splitting [10–12]. Among them, bismuth vanadate ($BiVO_4$) is one of the most promising and most studied candidates [13–15], due to its band gap being suitable for absorption of visible light [16] and a favorable band alignment with the OER [17,18]. $BiVO_4$ exhibits n-type conductivity [19]; however, electron trapping greatly limits carrier mobility and lowers PEC performance [20]. Conductivity and charge transfer can be increased by introducing charge carriers through doping, for example, by substituting V^{5+} with Mo^{6+} or W^{6+} [21] or by interstitial hydrogen [19,22]. Charges can also localize around intrinsic defects, such as oxygen vacancies [23–25], or through the formation of polarons [18,26–29]. In particular, the electron polaron has been found to have an energy level aligned with the OER and could potentially enhance the PEC performance [18]. In addition to doping and defects, the position of the CTL can also be tuned by applying strain [30]. Experimental measurements on epitaxial $BiVO_4$ thin films indicate that small biaxial strains (∼1%) can induce CTL shifts approaching 100 meV, making strain a promising route for tuning polaron levels [31]. While localized

*Contact author: ethan.berger@chalmers.se
†Contact author: julia.wiktor@chalmers.se

Published by the American Physical Society under the terms of the Creative Commons Attribution 4.0 International license. Further distribution of this work must maintain attribution to the author(s) and the published article's title, journal citation, and DOI. Funded by Bibsam.

electrons arising from polarons and oxygen vacancies play an important role in the water-splitting reaction, their stability, and energetic alignment under operando temperature and strain conditions remain largely unexplored.

Finite-temperature simulations rely on molecular dynamics (MD). In the context of CTLs, the free energy can be obtained through thermodynamic integration [32], which requires long simulations to obtain converged results. Additionally, large supercells are necessary when studying charged systems [33–35]. This makes the use of *ab initio* MD computationally impractical. In recent years, machine-learned interatomic potentials (MLIPs) have emerged as an efficient solution to perform long MD simulations for large numbers of atoms, routinely allowing nanoseconds-long simulations for millions of atoms [36–40]. While standard MLIPs are trained to predict energies and forces, there have also been MLIPs developed to predict other properties, such as electric dipoles [41,42], polarizabilities [43,44], or even electronic densities [45,46]. A few models that predict atomic charges have also been suggested, for example, based on partial charges [47,48], Born effective charges [49], or charges learned implicitly from electrostatics [50,51].

While these models have been successfully trained for the neutral charge state, their application to charged systems is not straightforward. One possibility is to treat different charge states by training separate models [52]. This approach is, however, limited in that it does not ensure convergence of the formation energies for large periodic systems [53], thereby restricting the system size to the one used during training. Instead, charge states can be modeled by distinguishing atoms near the localized charges by labeling them as different species depending on the total charge, effectively allowing them to adopt different oxidation states [53]. When combined with thermodynamic integration, the labeling approach has been successfully applied to study the temperature dependence of CTL in semiconductors [54] and is expected to be suitable for the study of electron polarons and oxygen vacancies in $BiVO_4$.

In this work, we investigate the stability of electron polarons and oxygen vacancies in $BiVO_4$ under realistic conditions through the use of a neuroevolution potential (NEP). Localized charges are treated by labeling atoms, which enables simulations across different charge states and greatly simplifies thermodynamic integrations. To closely match experimental conditions, free-energy differences and CTL are calculated at temperatures between 10 and 400 K, as well as under biaxial strains between -2% and 2%. For the oxygen vacancy, different localized sites are considered, revealing favored sites in the vicinity of the vacancy. Because of the strongly harmonic VO_4 units and cancellation of terms, the free-energy differences are found to be constant with temperature. As a result, the temperature dependence of the band edges is identified as the main source of variation in the CTL and formation energies with temperature, for both the electron polaron and the oxygen vacancy. In contrast, strain is found to impact the absolute position of the CTL and therefore can be used to tune the optical properties of $BiVO_4$.

II. METHODS

A. Electron polaron and oxygen vacancy in $BiVO_4$

The different atomic structures considered in this work are presented in Fig. 1. Scheelite $BiVO_4$ consists of isolated tetrahedral VO_4 units, with Bi atoms situated between them in an eightfold coordination environment [Fig. 1(a)]. Upon formation of an electron polaron, the excess charge localizes around a single vanadium site, leading to an elongation of the V–O bonds [Fig. 1(b)]. For an oxygen vacancy, removal of an O^{2-} anion perturbs the local environment, with the vanadium in the resulting VO_3 unit shifting toward a neighboring VO_4 and giving rise to the corner-sharing structure shown in Fig. 1(c). Because oxygen vacancies act as donor-type defects in oxides, an oxygen vacancy in $BiVO_4$ can occur in the $+2, +1$, or neutral charge state. The excess electrons localize on V sites to form one or two electron polarons so that the different charge states can be viewed as the vacancy coupled to zero, one, or two localized electrons [Figs. 1(c)–1(e)]. Note that electron localization can occur on different sites around an oxygen vacancy, with previous studies having sampled these different configurations using density functional theory (DFT) calculations [23,55].

B. Defect formation energy and charge-transition levels

The CTL is closely linked to the defect formation energy ΔF. In its most general form, it can be written as

$$\Delta F_q = \Delta G_q + \sum_i n_i \mu_i + q[\varepsilon_v + \varepsilon_F] + E_{\mathrm{corr}}, \qquad (1)$$

where ΔG is the free-energy difference between the pristine and defective systems, n_i is the number of atomic defects, μ_i is the chemical potential of atom i, q is the charge state, ε_F is the Fermi energy, ε_v is the location of the valence band maximum (VBM), and E_{corr} is the finite-size correction term. This latter term is neglected in this work for two reasons. First, this work focuses on the effect of temperature on the stability of localized charges, and the correction term is expected to be almost constant with temperature. Additionally, large cells are used for the DFT calculations, leading to a small correction term due to the large dielectric constant of $BiVO_4$. The charge-transition level $\varepsilon_{q/q'}$ between charge states q and q' can then be written as

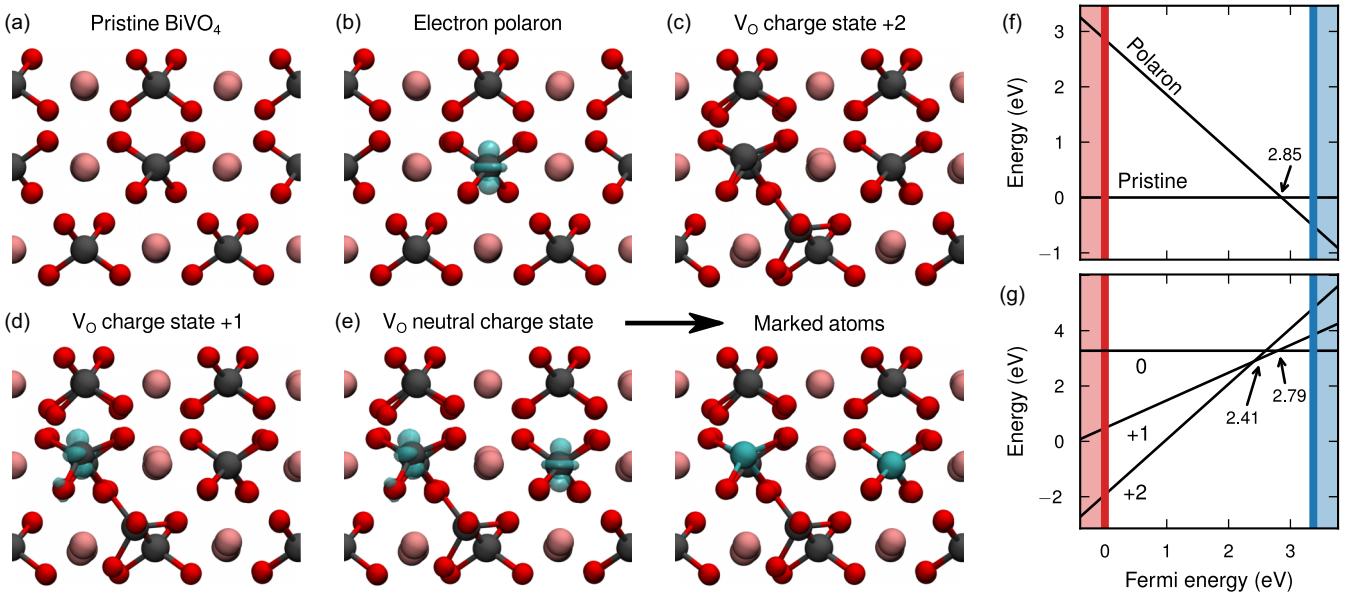

FIG. 1. Atomic structure of (a) pristine $BiVO_4$, (b) an electron polaron, and an oxygen vacancy in (c) charge state +2, (d) charge state +1, and (e) neutral charge state. For the latter, the labeling of atoms is also shown, with localized electrons (on the left) replaced by a separate V species (in blue on the right). (f)–(g) Formation energy diagrams of (f) the electron polaron and (g) the oxygen vacancy obtained using the labeled NEP model at 0 K. The VBM and CBM are shown using vertical lines, while arrows indicate the CTLs, with their values given in eV.

$$\varepsilon_{q/q'} = \frac{\Delta G_{q/q'}}{q' - q} - \varepsilon_v, \tag{2}$$

where $\Delta G_{q/q'} = \Delta G_q - \Delta G_{q'}$ is the free-energy difference between the two charge states. It should be noted that the free energy of the pristine system is not necessary to obtain CTLs of defective systems.

C. Neuroevolution potential and labeling of atoms

Finite-temperature MD simulations are performed using a neuroevolution potential (NEP) [56,57]. The model is trained using reference energies, forces, and stress calculated at the DFT level using the FHI-AIMS package [58–61]. The hybrid functional PBE0 with a mixing parameter of 0.14 is employed to obtain accurate band gaps and CTLs [28,29]. This value follows the generalized Koopmans' condition for localized charge states in $BiVO_4$ and is therefore well suited for describing the electron polarons and vacancy-bound localized electrons considered here. We note that previous work by some of the authors used a larger mixing parameter, around $\alpha = 0.22$, chosen to reproduce quasiparticle self-consistent GW band gaps. Changing α would affect the band gap, the absolute band-edge positions, and the CTLs, including their positions relative to the VBM. However, the main conclusions of the present work concern the temperature and strain dependence of free-energy differences. Once the localized defect level is stabilized within the band gap, these trends are expected to depend only weakly on the precise amount of exact exchange, because they are governed mainly by the local potential-energy surfaces of the localized charge states. The near-harmonic potential energy surfaces found here therefore suggest that the temperature independence of the free-energy differences should be robust with respect to moderate changes in α. Similarly, spin-orbit coupling (SOC) is not included in the present calculations. Previous work showed that SOC reduces the band gap of $BiVO_4$ by about 0.13 eV [62]. Since the electron-polaron states are mainly derived from V 3d states, the direct effect of SOC on the absolute CTL positions is expected to be smaller than its effect on the band gap. Its effect on the temperature and strain dependence of the CTLs is expected to be even smaller.

In the NEP model, localized electrons are treated by labeling atoms, similar to the method developed in Ref. [53] and successfully applied to charged defects in Ref. [54]. When considering the electron polaron and oxygen vacancies in $BiVO_4$, negative charges strongly localize at specific vanadium sites [25]. We therefore only label vanadium atoms, resulting in only one additional species denoted V^{4+}, while other vanadium atoms are labeled V^{5+}. A graphical representation of the labeling procedure is shown in Fig. 1(e). Note that having two electron polarons on the same site is found to be one of the most stable electronic states for the oxygen vacancy [23,55]. Including this electronic configuration to the labeling would require adding an additional specie V^{3+} and effectively make the NEP model more complex. We therefore restrict ourselves to configurations with electrons

on distinct V sites. It is important to note that the labeling scheme used in this work does not capture migration/hopping of localized charges and therefore treats the localization sites as static.

A first generation of NEP model is trained using rattled structures as well as snapshots from *ab initio* MD from Ref. [18]. Additional structures were iteratively added to the training set using active learning and committee error estimates. The data acquisition workflow is presented in more detail in Fig. S1 in Supplemental Material [63]. To ensure consistent labeling, we only select structures where V^{4+} atoms have a Hirshfeld spin moment higher than 0.5. As a result, the final training set contains 973 structures, including 18 6221 atoms in total and 774 V^{4+} atoms. The quality of the dataset is further assessed using principal component analysis, as presented in Fig. S2 in Supplemental Material [63]. The final resulting model shows root mean square error of 2.74 meV/atom, 115 meV/Å, and 12.1 meV/atom for the energies, forces, and virials, respectively. Further metrics for assessing the accuracy of the model are discussed and presented in Fig. S3 in Supplemental Material [63]. Note that the force error is the largest for the marked atoms (299 meV/Å), mostly due to their underrepresentation within the training data. Despite this, the model still closely reproduces the formation energy of the electron polaron and the oxygen vacancy, which are presented in Figs. 1(f) and 1(g). For the electron polaron, we find a formation energy of −514 meV and a CTL at 2.85 eV, which agrees well with our own DFT values of −584 meV and 2.78 eV as well as other previous DFT calculations [28,29]. For oxygen vacancies, the two CTLs are found at 2.41 and 2.79 eV for $\varepsilon_{+1/+2}$ and $\varepsilon_{0/+1}$ respectively. Additionally, the model also correctly predicts the increased V–O bond length in the presence of a polaron, going from 1.72 to 1.8 Å, again in good agreement with previous DFT calculations [28] as well as *ab initio* MD [27].

D. Thermodynamic integration

Free-energy differences at finite temperature are obtained through nonequilibrium thermodynamic integration [32],

$$\Delta G = \int_0^{t_s} \left[H_f(t) - H_i(t)\right] \frac{\mathrm{d}\lambda}{\mathrm{d}t}\,\mathrm{d}t, \tag{3}$$

where ΔG is the free-energy difference between the Hamiltonians H_i and H_f. To obtain a reference free energy, an Einstein crystal is typically used as one of the Hamiltonians, resulting in the Frenkel-Ladd path [65]. In this work, H_i and H_f denote two versions of the NEP model, in which the marked atoms are either treated as V^{4+} or V^{5+}, thereby allowing a continuous path between charge states. Combining marked atoms with thermodynamic integration has already been successfully applied to charged defects in several materials [54]. Free energies are obtained by first equilibrating the initial charge state for 20 ps in the NPT ensemble at the target temperature. To reduce errors, we use the mean between the forward and backward processes. Free energies are obtained by running thermodynamic integration for 100 ps in both forward and backward directions. To avoid finite-size effects, we use $8\sqrt{2} \times 8\sqrt{2} \times 2$ supercells containing 12 288 atoms. The convergence of ΔG with the simulation length and the supercell size is benchmarked and discussed in Figs. S4 and S5 in Supplemental Material [63]. Finally, to reduce noise from the finite length of the thermodynamic integration, the free-energy differences are obtained from the average over 10 MD runs. Note that the standard deviation is found to be at most 5 meV, far smaller than the energy range considered in this work.

III. RESULTS

A. Temperature and strain dependence of electron polaron free energies

Combining our marked NEP model with Eq. (3) enables efficient computation of free energies. To better recreate experimental conditions [30,31], all results pertaining to strain are obtained at 300 K and with biaxial strain along the [100] and [010] directions. The temperature dependence of the electron polaron free-energy difference (ΔG_e) as well as CBM, and VBM are presented in Fig. 2(a). ΔG_e is found to be constant with temperature at 2.83 eV above the VBM at 0 K, with small fluctuations of 2 meV, likely due to finite length of the thermodynamic integration. When applying strain instead, ΔG_e shifts at a rate of −46 meV/%, as shown in Fig. 2(b).

The difference in behavior can be explained by examining the potential energy surface (PES) as a function of the V–O bond length at 0 K, as shown in Fig. 2(c). The corresponding vertical transition energies are 3.45 and 2.17 eV for the absorption and emission, respectively. The effect of temperature on the vertical transitions of the electron polaron and the oxygen vacancy is discussed in Fig. S6 in Supplemental Material [63]. In all cases, the vertical transitions are temperature-independent, with temperature mainly broadening the distribution through thermal fluctuations. Note that comparison with experimental vertical transitions can be difficult because the band gap is sensitive to many-body interactions, nuclear quantum effects, and spin-orbit coupling [62]. From Fig. 2(c), the PESs of V^{5+} and V^{4+} along the V–O bonds are found to be harmonic with similar curvatures. The harmonicity is reflected in the V–O radial distribution functions (RDFs), shown in Fig. 2(d) as a function of temperature and in Fig. 2(e) as a function of strain. At low temperature, sharp peaks appear around 1.72 and 1.80 Å for V^{5+} and V^{4+}, respectively, as expected from the PES.

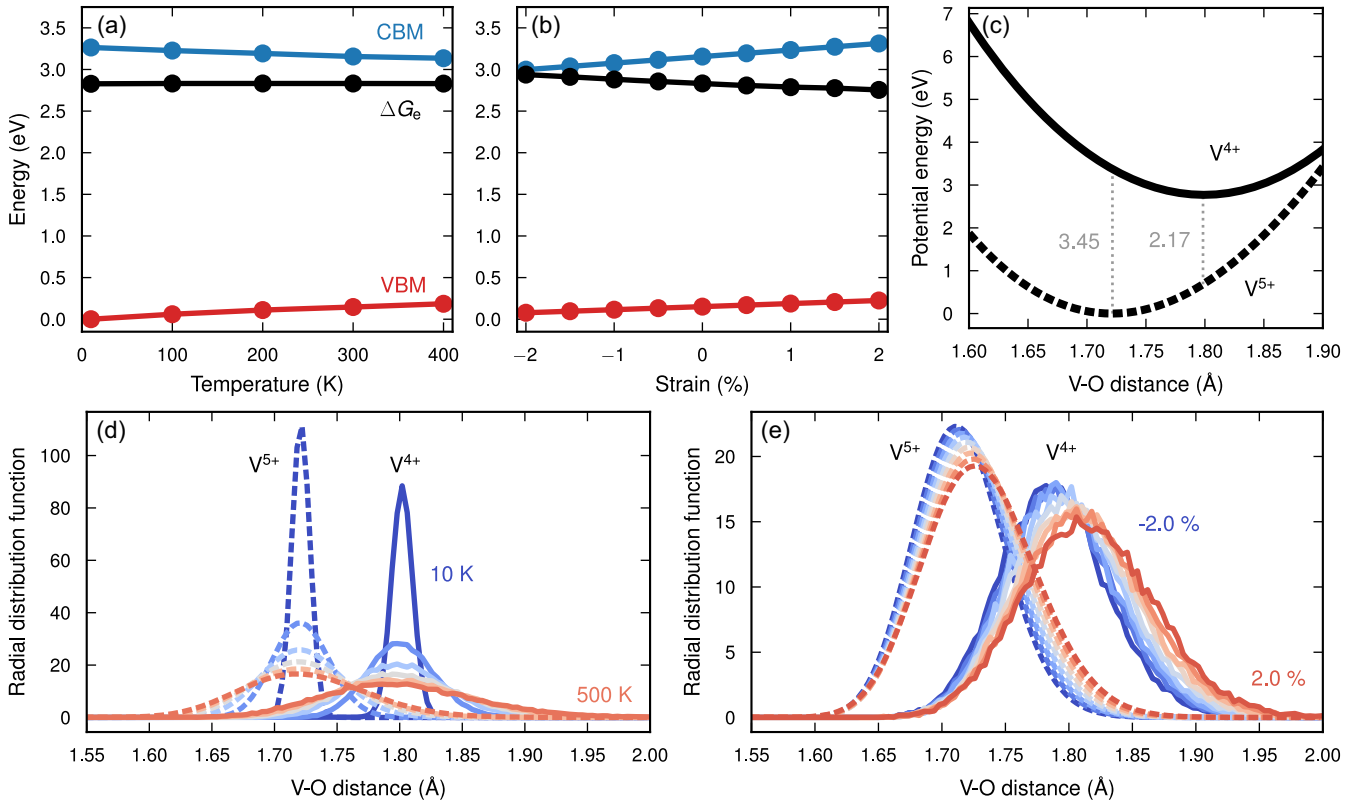

FIG. 2. Band edges and free-energy difference of the electron polaron ΔG_e as a function of (a) temperature and (b) strain. (c) Potential energy surface along the V–O bond distance for V^{4+} and V^{5+}. The emission and absorption vertical transitions are shown in gray, with their value given in eV. Radial distribution function of V–O pairs for V^{4+} and V^{5+} at (d) various temperatures and (e) various strains.

With increasing temperature, the peaks broaden but remain symmetric, indicating weak anharmonicity. Additionally, the average bond lengths remain constant, with fluctuations of the order of 3×10^{-3} Å over the entire temperature range. While the harmonic PESs lead to symmetric RDFs with temperature-invariant mean bond lengths, their similar curvatures ensure that vibrational contributions largely cancel between V^{5+} and V^{4+}. Together, these effects explain why both the vertical transition energies and the free-energy difference ΔG_e are temperature-independent. Similar behavior was reported for the optical defect level in $CsBrCl_3$ [52], while thermal fluctuations of the free-energy difference are observed for defects in materials with anharmonic PESs [54]. Despite the average V–O bond length remaining constant, we still observe a thermal expansion of 3.94×10^{-5} K^{-1} (see Fig. S7 in Supplemental Material [63]), in good agreement with experiment [66]. The change of volume induced by thermal expansion likely arises from elongation of Bi–O bonds and/or increased spacing between VO_4 units, and accordingly has a negligible effect on the stability of the electron polaron.

In contrast, strain clearly impacts the peak position of the RDF, as represented in Fig. 2(e). The V–O bond length decreases with compressive strain, and increases with tensile strain, as can be seen from the RDF in Fig. 2(e). The movement of RDF peaks can be attributed to a shift of the V^{4+} PES under strain (see Fig. S8 in Supplemental Material [63]), which has already been suggested from experimental measurements [31]. Interestingly, the PES and the RDF peaks remain largely symmetric under strain despite the variation in bond length, consistent with the weak anharmonicity already observed in the absence of strain. The structural origin of this behavior is likely related to the fact that electron localization mainly shifts the preferred V–O bond length, without substantially changing the local V–O stiffness. As a result, the V^{5+} and V^{4+} states sample similar, nearly harmonic wells, such that increasing temperature mostly broadens the bond-length distributions without changing the free-energy difference. Biaxial strain, in contrast, changes the equilibrium geometry of the surrounding lattice and can therefore change how favorably the longer-bond V^{4+} configuration is accommodated relative to V^{5+}.

B. Configurational sampling of oxygen-vacancy charge states

For oxygen vacancies, the formation energies of charge states +1 and 0 depend on which vanadium sites the

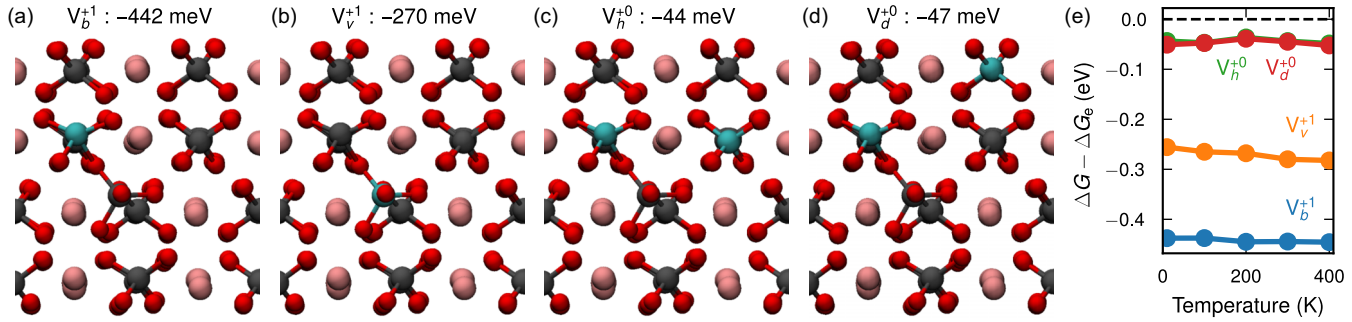

FIG. 3. Atomic structures of oxygen vacancies in (a),(b) charge state +1 and (c),(d) the neutral charge state. The vanadium sites with localized electrons are shown in cyan. (e) Free-energy differences for each structure as a function of temperature. Note that the free energy differences are shifted by the polaron free-energy difference (ΔG_e) for comparison.

electrons localize on. Previous studies already investigated the variation with sites for oxygen vacancies both in bulk [23] and at the interface [24]. By leveraging the high efficiency of NEP, we can also sample different configurations and further investigate their temperature dependence. In charge state +1, only one electron localizes around the vacancy. Here, we study all vanadium sites within a 10 Å radius around the oxygen vacancy, as well as the electron localizing far away from the vacancy (detailed results are presented in Fig. S9 in Supplemental Material [63]). Note that the free-energy differences are presented with respect to ΔG_e for an easier comparison with the electron polaron. In fact, the free-energy difference of having an electron far from the vacancy is equal to ΔG_e, correctly showing the dissociation between the oxygen vacancy and the localized electron. The two configurations leading to the lowest free-energy difference are highlighted in Figs. 3(a) and 3(b). In particular, they correspond to the two sites on each side of the oxygen vacancy, with free-energy differences of 270 and 442 meV below ΔG_e at 300 K for the corner-sharing VO_3 and VO_4 units, respectively. This result highlights how oxygen vacancies can increase charge localization in $BiVO_4$.

In the neutral charge state, a second electron becomes localized, meaning that a second atom has to be marked in our simulations. For simplicity, we consider one fixed electron at the corner-sharing VO_4 and sample every other vanadium site in a 10 Å radius around the oxygen vacancy. While localization on most of the sites close to the vacancy leads to a positive free-energy difference (see Fig. S9 in Supplemental Material [63]), two sites have a small negative free-energy difference. These two configurations, shown in Figs. 3(c) and 3(d), have already been separately identified through DFT calculations in Refs. 25 and 23, respectively. Interestingly, electrons localizing on each side of the vacancy is not favorable, although these two sites previously had the lowest free-energy difference.

Finally, Fig. 3(e) shows the free-energy difference with temperature of the configurations presented in Figs. 3(a)–3(d). Similar to the electron polaron, the free-energy differences for the oxygen vacancy $\Delta G_{+1/+2}$ and $\Delta G_{0/+1}$ are found to be constant with temperature in all configurations. This result also holds for configurations with higher free- energy differences, as can be seen from Fig. S9 in Supplemental Material [63]. Conclusions from previous DFT calculations are therefore expected to remain valid at finite temperature. In particular, although it cannot be accessed with the current model, the configuration in which both excess electrons localize on the same V site may also exhibit only a minor temperature dependence.

C. Temperature and strain dependence of CTLs

Using the results for the free-energy differences, along with the dependence of the VBM shown in Figs. 2(a) and 2(b), we can determine the movement of the CTLs with temperature and strain. Figures 4(a) and 4(b) shows the CTLs relative to the temperature- and strain-dependent VBM. This representation is most relevant for comparison to optical absorption/emission and spectroscopic measurements, which probe transition energies relative to the band edges. In contrast, Fig. 4(c) shows the absolute CTLs within the band gap, which are relevant when assessing the band alignment with the OER. This representation also provides additional insights by clearly separating the contributions arising from the free-energy differences or from shifts of the band edges. When considering only the effect of temperature, it is clear that the absolute position of the CTL is constant, while variations of the band edges dominate. We find a band gap of 3.26 eV at 10 K, which decreases to 3.01 eV at 300 K. This value is still higher than the experimental one, consistent with the absence of many-body interaction, nuclear quantum motion, and spin-orbit coupling [62]. However, we find that the band gap decreases at a rate of 0.86 meV/K, in good agreement with experimental observations [66]. The band-gap

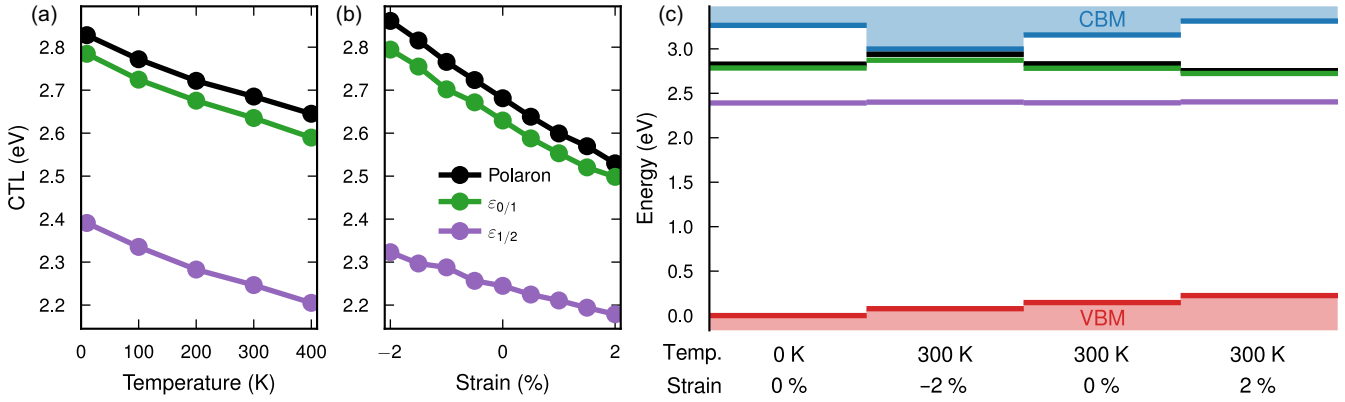

FIG. 4. Charge-transition levels of the electron polaron and oxygen vacancy with respect to the (a) temperature-dependent VBM and (b) strain-dependent VBM. (c) Comparison between energy levels within the band gap at various temperatures and strains.

decrease also leads to a shift of 146 meV in the VBM, as well as in all CTLs. At 10 K, CTLs of 2.82, 2.78, and 2.39 eV are found for the electron polaron, $\varepsilon_{0/+1}$ and $\varepsilon_{+1/+2}$, which shift to 2.67, 2.64, and 2.25 eV at 300 K. Also note that the shift of the CBM with temperature leads to an increase in the formation energy, going from −436 meV at 10 K to −324 meV at 300 K for the polaron.

Strain is found to have a larger effect on the CTL position than temperature. From Fig. 4(c), it is clear that the energy level of the polaron, as well as both band edges, are strain-dependent. As a result, the polaron CTL shifts at a rate of −83 meV/%, in good agreement with experimental measurements [31]. Interestingly, the absolute CTL $\varepsilon_{+1/+2}$ shows no dependence on strain and is therefore only impacted by the movement of the VBM, whereas $\varepsilon_{0/+1}$ follows the same behavior as the polaron level. Additionally, large shifts of the CBM occur under strain, which directly impacts the formation energy of the polaron. For example, the formation energy goes from −324 meV without strain to −60 meV and −558 meV at −2% and +2%, respectively. Note that compressive strain strongly increases the polaron formation energy, such that at sufficiently large strain, polaron formation is expected to become energetically unfavorable.

The movement of the electron polaron CTL with temperature can be compared with previous *ab initio* MD results from Ref. [18]. In this previous work, the CTL is found to move from 2.52 eV at 0 K to 1.81 eV at 300 K. This shift arises from variation in both the VBM and the free-energy difference, in strong contrast with the current results. One of the main differences is the use of a larger mixing parameter in the hybrid functional, namely 25% compared to 14% in this work. This leads to a larger band gap, as well as a lower formation energy and consequently a lower CTL. The shift of the band gap with temperature is also larger, with a shift of the VBM of 0.51 eV compared to 0.14 eV in this work. In Ref. [27], the same lattice constant is used at 0 and 300 K, resulting in a downward shift of 0.21 eV of the polaron energy level. In contrast, our thermodynamic integrations are performed after equilibration in the NPT ensemble, effectively accounting for thermal expansion. Results with NVT equilibration are presented in Fig. S10 in Supplemental Material [63] and show an upward shift of 63 meV. While differences can be found between our results and previous *ab initio* MD, they can mostly be explained by differences in the simulation methods, namely the fraction of Hartree-Fock exchange used in the hybrid functional and the use of fixed or relaxed lattice constants. The latter effect further highlights the usefulness of machine-learned interatomic potentials for assessing the temperature dependence of charge-localization stability, as they enable efficient convergence testing with respect to key simulation details. Both sets of results also agree on the fact that the variation in the CTL with temperature mainly arises from shifts of the band edges.

IV. CONCLUSION

In conclusion, we trained a neuroevolution potential for $BiVO_4$ capable of modeling localized charges associated with electron polarons and oxygen vacancies. The potential is used in combination with thermodynamic integration to obtain free energies and charge-transition levels at finite temperature and under strain. For the electron polaron, the free-energy difference is found to be constant with temperature because of the strongly harmonic VO_4 units. In contrast, strain modifies the potential energy surfaces of V^{5+} and V^{4+}, thereby affecting the free-energy difference. The method is also used to sample various localization sites around an oxygen vacancy, revealing favored sites that remain stable at high temperatures. Consequently, variations of the charge-transition levels of the electron polaron and the oxygen vacancy are found to arise solely from an upward shift of the VBM with temperature. Similarly, the polaron formation energies are

found to increase due to a downshift of the CBM, showing the importance of band-edge fluctuations. Strain is also found to shift the CTL of the polaron and the oxygen vacancy. As a result, strain can be used to modify the position of the CTLs and tune the optoelectronic properties of $BiVO_4$. Our results show that defect-state alignment in $BiVO_4$ is intrinsically robust against temperature while remaining highly tunable through strain, thereby providing a clearer framework for interpreting spectroscopy and designing improved photoanodes under operando conditions. Since dopants such as Mo, W, and Cr have been shown to affect electron-polaron localization in $BiVO_4$ [67,68], it would be interesting in future work to determine whether charge trapping at or near dopants exhibits the same weak temperature dependence and strain response as the intrinsic localized states studied here.

ACKNOWLEDGMENTS

This work was supported by the Swedish Strategic Research Foundation through a Future Research Leader programme (FFL21-0129), the Swedish Research Council (2019-03993), the European Research Council (ERC Starting Grant No. 101162195), the Knut and Alice Wallenberg Foundation (No. 2023.0032). The computations were enabled by resources provided by the National Academic Infrastructure for Supercomputing in Sweden (NAISS) at C3SE, PDC, and NSC, partially funded by the Swedish Research Council through Grant Agreement No. 2022-06725.

DATA AVAILABILITY

The data that support the findings of this article are openly available [69].

[1] A. Fujishima and K. Honda, *Electrochemical photolysis of water at a semiconductor electrode*, Nature (London) **238**, 37 (1972).

[2] M. G. Walter, E. L. Warren, J. R. McKone, S. W. Boettcher, Q. Mi, E. A. Santori, and N. S. Lewis, *Solar water splitting cells*, Chem. Rev. **110**, 6446 (2010).

[3] W. Yang, R. R. Prabhakar, J. Tan, S. D. Tilley, and J. Moon, *Strategies for enhancing the photocurrent, photovoltage, and stability of photoelectrodes for photoelectrochemical water splitting*, Chem. Soc. Rev. **48**, 4979 (2019).

[4] X. Zhang and A. Bieberle-Hütter, *Modeling and simulations in photoelectrochemical water oxidation: From single level to multiscale modeling*, ChemSusChem **9**, 1223 (2016).

[5] H. Matsuo, Y. Noguchi, and M. Miyayama, *Gap-state engineering of visible-light-active ferroelectrics for photovoltaic applications*, Nat. Commun. **8**, 207 (2017).

[6] H.-P. Komsa and A. V. Krasheninnikov, *Native defects in bulk and monolayer* MoS_2 *from first principles*, Phys. Rev. B **91**, 125304 (2015).

[7] S. Qiao, Y.-N. Wu, X. Yan, B. Monserrat, S.-H. Wei, and B. Huang, *Temperature effect on charge-state transition levels of defects in semiconductors*, Phys. Rev. B **105**, 115201 (2022).

[8] C. Franchini, M. Reticcioli, M. Setvin, and U. Diebold, *Polarons in materials*, Nat. Rev. Mater. **6**, 560 (2021).

[9] M. Baskurt and J. Wiktor, *Charge localization in* $Cs_2AgBiBr_6$ *double perovskite: Small polarons and self-trapped excitons*, J. Phys. Chem. C **127**, 23966 (2023).

[10] C. Janáky, K. Rajeshwar, N. R. de Tacconi, W. Chanmanee, and M. N. Huda, *Tungsten-based oxide semiconductors for solar hydrogen generation*, Catal. Today **199**, 53 (2013).

[11] M. Kapilashrami, Y. Zhang, Y.-S. Liu, A. Hagfeldt, and J. Guo, *Probing the optical property and electronic structure of* TiO_2 *nanomaterials for renewable energy applications*, Chem. Rev. **114**, 9662 (2014).

[12] K. Sivula and R. van de Krol, *Semiconducting materials for photoelectrochemical energy conversion*, Nat. Rev. Mater. **1**, 15010 (2016).

[13] J. H. Kim and J. S. Lee, *Elaborately modified* $BiVO_4$ *photoanodes for solar water splitting*, Adv. Mater. **31**, 1806938 (2019).

[14] B. D. Nguyen, I.-H. Choi, and J.-Y. Kim, *Strategies for enhancing* $BiVo_4$ *photoanodes for pec water splitting: A state-of-the-art review*, Nanomaterials **15**, 1494 (2025).

[15] B. Liu, X. Wang, Y. Zhang, M. Zhu, C. Zhang, S. Li, Y. Ma, W. Huang, and S. Wang, *A standalone bismuth vanadate-silicon artificial leaf achieving 8.4% efficiency for hydrogen production*, Nat. Commun. **16**, 2792 (2025).

[16] J. K. Cooper, S. Gul, F. M. Toma, L. Chen, Y.-S. Liu, J. Guo, J. W. Ager, J. Yano, and I. D. Sharp, *Indirect bandgap and optical properties of monoclinic bismuth vanadate*, J. Phys. Chem. C **119**, 2969 (2015).

[17] J. K. Cooper, S. Gul, F. M. Toma, L. Chen, P.-A. Glans, J. Guo, J. W. Ager, J. Yano, and I. D. Sharp, *Electronic structure of monoclinic* $BiVO_4$, Chem. Mater. **26**, 5365 (2014).

[18] J. Wiktor, F. Ambrosio, and A. Pasquarello, *Role of polarons in water splitting: The case of* $BiVO_4$, ACS Energy Lett. **3**, 1693 (2018).

[19] J. K. Cooper, S. B. Scott, Y. Ling, J. Yang, S. Hao, Y. Li, F. M. Toma, M. Stutzmann, K. V. Lakshmi, and I. D. Sharp, *Role of hydrogen in defining the n-type character of* $BiVO_4$ *photoanodes*, Chem. Mater. **28**, 5761 (2016).

[20] F. F. Abdi, T. J. Savenije, M. M. May, B. Dam, and R. van de Krol, *The origin of slow carrier transport in* $BiVO_4$ *thin film photoanodes: A time-resolved microwave conductivity study*, J. Phys. Chem. Lett. **4**, 2752 (2013).

[21] K. P. S. Parmar, H. J. Kang, A. Bist, P. Dua, J. S. Jang, and J. S. Lee, *Photocatalytic and photoelectrochemical water oxidation over metal-doped monoclinic* $BiVO_4$ *photoanodes*, ChemSusChem **5**, 1926 (2012).

[22] G. Wang, Y. Ling, X. Lu, F. Qian, Y. Tong, J. Z. Zhang, V. Lordi, C. Rocha Leao, and Y. Li, *Computational and photoelectrochemical study of hydrogenated bismuth vanadate*, J. Phys. Chem. C **117**, 10957 (2013).

[23] H. Seo, Y. Ping, and G. Galli, *Role of point defects in enhancing the conductivity of* $BiVO_4$, Chem. Mater. **30**, 7793 (2018).

[24] W. Wang, P. J. Strohbeen, D. Lee, C. Zhou, J. K. Kawasaki, K.-S. Choi, M. Liu, and G. Galli, *The role of surface oxygen vacancies in* $BiVO_4$, Chem. Mater. **32**, 2899 (2020).
[25] N. Österbacka, F. Ambrosio, and J. Wiktor, *Charge localization in defective* $BiVO_4$, J. Phys. Chem. C **126**, 2960 (2022).
[26] A. J. E. Rettie, W. D. Chemelewski, J. Lindemuth, J. S. McCloy, L. G. Marshall, J. Zhou, D. Emin, and C. B. Mullins, *Anisotropic small-polaron hopping in W:* $BiVO_4$ *single crystals*, Appl. Phys. Lett. **106**, 022106 (2015).
[27] J. Wiktor and A. Pasquarello, *Electron and hole polarons at the* $BiVO_4$*–water interface*, ACS Appl. Mater. Interfaces **11**, 18423 (2019).
[28] S. Falletta and A. Pasquarello, *Polarons free from many-body self-interaction in density functional theory*, Phys. Rev. B **106**, 125119 (2022).
[29] T. Möslinger, N. Österbacka, and J. Wiktor, *Competing self-trapped exciton states and multiple emission pathways in* $BiVO_4$, J. Phys. Chem. Lett. **16**, 6861 (2025).
[30] E. N. Fernandez, R. van de Krol, and F. F. Abdi, *Tuning the optical and photoelectrochemical properties of epitaxial* $BiVO_4$ *by lattice strain*, Small Struct. **5**, 2400097 (2024).
[31] E. N. Fernandez, D. A. Grave, R. van de Krol, and F. F. Abdi, *Strain-induced distortions modulate the optoelectronic properties of epitaxial* $BiVO_4$ *films*, Adv. Energy Mater. **13**, 2301075 (2023).
[32] R. Freitas, M. Asta, and M. de Koning, *Nonequilibrium free-energy calculation of solids using lammps*, Comput. Mater. Sci. **112**, 333 (2016).
[33] C. Freysoldt, Jörg Neugebauer, and C. G. Van de Walle, *Fully ab initio finite-size corrections for charged-defect supercell calculations*, Phys. Rev. Lett. **102**, 016402 (2009).
[34] H.-P. Komsa, T. T. Rantala, and A. Pasquarello, *Finite-size supercell correction schemes for charged defect calculations*, Phys. Rev. B **86**, 045112 (2012).
[35] Y. Kumagai and F. Oba, *Electrostatics-based finite-size corrections for first-principles point defect calculations*, Phys. Rev. B **89**, 195205 (2014).
[36] V. L. Deringer, M. A. Caro, and Gábor Csányi, *Machine learning interatomic potentials as emerging tools for materials science*, Adv. Mater. **31**, 1902765 (2019).
[37] Jörg Behler, *Four generations of high-dimensional neural network potentials*, Chem. Rev. **121**, 10037 (2021).
[38] Z. Fan, Y. Wang, P. Ying, K. Song, J. Wang, Y. Wang, Z. Zeng, K. Xu, E. Lindgren, J. M. Rahm, A. J. Gabourie, J. Liu, H. Dong, J. Wu, Y. Chen, Z. Zhong, J. Sun, P. Erhart, Y. Su, and T. Ala-Nissila, *Gpumd: A package for constructing accurate machine-learned potentials and performing highly efficient atomistic simulations*, J. Chem. Phys. **157**, 114801 (2022).
[39] G. Wang, C. Wang, X. Zhang, Z. Li, J. Zhou, and Z. Sun, *Machine learning interatomic potential: Bridge the gap between small-scale models and realistic device-scale simulations*, iScience **27**, 109673 (2024).
[40] R. Jinnouchi and S. Minami, *Machine learning force fields in electrochemistry: From fundamentals to applications*, ACS Nano **19**, 22600 (2025).
[41] M. Veit, D. M. Wilkins, Y. Yang, R. A. DiStasio Jr., and M. Ceriotti, *Predicting molecular dipole moments by combining atomic partial charges and atomic dipoles*, J. Chem. Phys. **153**, 024113 (2020).
[42] N. Xu, P. Rosander, C. Schäfer, E. Lindgren, N. Österbacka, M. Fang, W. Chen, Y. He, Z. Fan, and P. Erhart, *Tensorial properties via the neuroevolution potential framework: Fast simulation of infrared and raman spectra*, J. Chem. Theory Comput. **20**, 3273 (2024).
[43] E. Berger and H.-P. Komsa, *Polarizability models for simulations of finite temperature raman spectra from machine learning molecular dynamics*, Phys. Rev. Mater. **8**, 043802 (2024).
[44] E. Berger, J. Niemelä, O. Lampela, Aé H. Juffer, and H.-P. Komsa, *Raman spectra of amino acids and peptides from machine learning polarizabilities*, J. Chem. Inf. Model. **64**, 4601 (2024).
[45] A. M. Lewis, A. Grisafi, M. Ceriotti, and M. Rossi, *Learning electron densities in the condensed phase*, J. Chem. Theory Comput. **17**, 7203 (2021).
[46] A. M. Lewis, P. Lazzaroni, and M. Rossi, *Predicting the electronic density response of condensed-phase systems to electric field perturbations*, J. Chem. Phys. **159**, 014103 (2023).
[47] N. Artrith, T. Morawietz, and Jörg Behler, *High-dimensional neural-network potentials for multicomponent systems: Applications to zinc oxide*, Phys. Rev. B **83**, 153101 (2011).
[48] T. Morawietz, V. Sharma, and J. Behler, *A neural network potential-energy surface for the water dimer based on environment-dependent atomic energies and charges*, J. Chem. Phys. **136**, 064103 (2012).
[49] S. Falletta, A. Cepellotti, A. Johansson, C. W. Tan, M. L. Descoteaux, A. Musaelian, C. J. Owen, and B. Kozinsky, *Unified differentiable learning of electric response*, Nat. Commun. **16**, 4031 (2025).
[50] P. Zhong, D. Kim, D. S. King, and B. Cheng, *Machine learning interatomic potential can infer electrical response*, npj Comput. Mater. **11**, 384 (2025).
[51] Z. Fan, B. Tang, E. Berger, E. Berger, E. Fransson, K. Xu, Z. Yan, Z. Liu, Z. Song, H. Dong, S. Chen, L. Li, Z. Wang, Y. Zhu, J. Wiktor, and P. Erhart, *qNEP: A highly efficient neuroevolution potential with dynamic charges for large-scale atomistic simulations*, arXiv:2601.19034.
[52] I. Mosquera-Lois and A. Walsh, *Dynamic vacancy levels in* $CsPbCl_3$ *obey equilibrium defect thermodynamics*, PRX Energy **4**, 043008 (2025).
[53] C. Linderälv, N. Österbacka, J. Wiktor, and P. Erhart, *Optical line shapes of color centers in solids from classical autocorrelation functions*, npj Comput. Mater. **11**, 101 (2025).
[54] T. Hainer, E. Berger, E. Berger, O. Hildeberg, P. Erhart, and J. Wiktor, *Thermal stabilization of defect charge states and finite-temperature charge transition levels*, arXiv:2512.15463.
[55] N. Österbacka and J. Wiktor, *Influence of oxygen vacancies on the structure of* $BiVO_4$, J. Phys. Chem. C **125**, 1200 (2021).
[56] Z. Fan, Z. Zeng, C. Zhang, Y. Wang, K. Song, H. Dong, Y. Chen, and T. Ala-Nissila, *Neuroevolution machine learning*

potentials: Combining high accuracy and low cost in atomistic simulations and application to heat transport, Phys. Rev. B **104**, 104309 (2021).

[57] K. Song *et al.*, *General-purpose machine-learned potential for 16 elemental metals and their alloys*, Nat. Commun. **15**, 10208 (2024).

[58] V. Blum, R. Gehrke, F. Hanke, P. Havu, V. Havu, X. Ren, K. Reuter, and M. Scheffler, *Ab initio molecular simulations with numeric atom-centered orbitals*, Comput. Phys. Commun. **180**, 2175 (2009).

[59] X. Ren, P. Rinke, V. Blum, J. Wieferink, A. Tkatchenko, A. Sanfilippo, K. Reuter, and M. Scheffler, *Resolution-of-identity approach to Hartree–Fock, hybrid density functionals, RPA, MP2 and GW with numeric atom-centered orbital basis functions*, New J. Phys. **14**, 053020 (2012).

[60] F. Knuth, C. Carbogno, V. Atalla, V. Blum, and M. Scheffler, *All-electron formalism for total energy strain derivatives and stress tensor components for numeric atom-centered orbitals*, Comput. Phys. Commun. **190**, 33 (2015).

[61] A. C. Ihrig, J. Wieferink, I. Y. Zhang, M. Ropo, X. Ren, P. Rinke, M. Scheffler, and V. Blum, *Accurate localized resolution of identity approach for linear-scaling hybrid density functionals and for many-body perturbation theory*, New J. Phys. **17**, 093020 (2015).

[62] J. Wiktor, I. Reshetnyak, F. Ambrosio, and A. Pasquarello, *Comprehensive modeling of the band gap and absorption spectrum of* $BiVO_4$, Phys. Rev. Mater. **1**, 022401 (2017).

[63] See Supplemental Material at http://link.aps.org/supplemental/10.1103/xwxv-6s55 for additional details such as data acquisition workflow, training of the neuroevolution potential, convergence of the free-energy difference with simulation length and supercell size, temperature dependence of the vertical transitions, thermal expansion, effect of strain on the potential energy surface, configurational sampling of oxygen-vacancy charge states, and difference between NPT and NVT equilibration, which includes Ref. [64].

[64] Z. Yan, Z. Fan, and Y. Zhu, *Improving robustness and training efficiency of machine-learned potentials by incorporating short-range empirical potentials*, J. Chem. Inf. Model. **66**, 1406 (2026).

[65] D. Frenkel and A. J. C. Ladd, *New Monte Carlo method to compute the free energy of arbitrary solids. Application to the fcc and hcp phases of hard spheres*, J. Chem. Phys. **81**, 3188 (1984).

[66] C. Hill, M. C. Weber, J. Lehmann, T. Leinen, M. Fiebig, J. Kreisel, and M. Guennou, *Role of the ferroelastic strain in the optical absorption of* $BiVO_4$, APL Mater. **8**, 081108 (2020).

[67] J. Cen, S. Li, J. Zheng, and F. Pan, *Electron polarons in the subsurface layer of* Mo/W*-doped* $BiVO_4$ *surfaces*, RSC Adv. **9**, 819 (2019).

[68] A. Ngoipala, L. Ngamwongwan, I. Fongkaew, S. Jungthawan, P. Hirunsit, S. Limpijumnong, and S. Suthirakun, *On the enhanced reducibility and charge transport properties of phosphorus-doped* $BiVO_4$ *as photocatalysts: A computational study*, J. Phys. Chem. C **124**, 4352 (2020).

[69] E. Berger, T. Hainer, T. Möslinger, P. Erhart, and J. Wiktor, *Stability of polarons and oxygen vacancies in* $BiVO_4$ *revealed by machine-learning-driven simulations* (2026), 10.5281/zenodo.19369114.

Supporting Information : Stability of Polarons and Oxygen Vacancies in $BiVO_4$ Revealed by Machine-Learning Driven Simulations

Ethan Berger,* Tobias Hainer, Tobias Möslinger, Paul Erhart, and Julia Wiktor†
Department of Physics and Astronomy, Chalmers University of Technology, SE-41296 Gothenburg, Sweden

I. DATA ACQUISITION WORKFLOW

A detailed breakdown of the number of structure in each NEP generation in presented in Fig. S1. Starting from DFT relaxed structures, the first NEP generation is trained using a total of 284 rattled structures. We then perform four cycles of active learning, where structures are selected using committee error estimates, as implemented in GPUMD. The final model is trained on a dataset of 973 structures, containing 186 221 atoms in total and 774 V^{4+} atoms.

The resulting training configurations cover the relevant structures visited during MD, as can be seen from the PCA in Fig. S2.

	Initial model	**Active learning**				**Final model**
	Rattled structures	Cycle 1	Cycle 2	Cycle 3	Cycle 4	Total
Pristine	80	50	0	10	50	190
Polaron	78	50	0	10	50	188
O Vac. +2	41	50	50	10	50	201
O Vac. +1	42	49	51	10	50	202
O Vac. +0	43	47	54	8	40	192

FIG. S1. Summary of the data acquisition workflow.

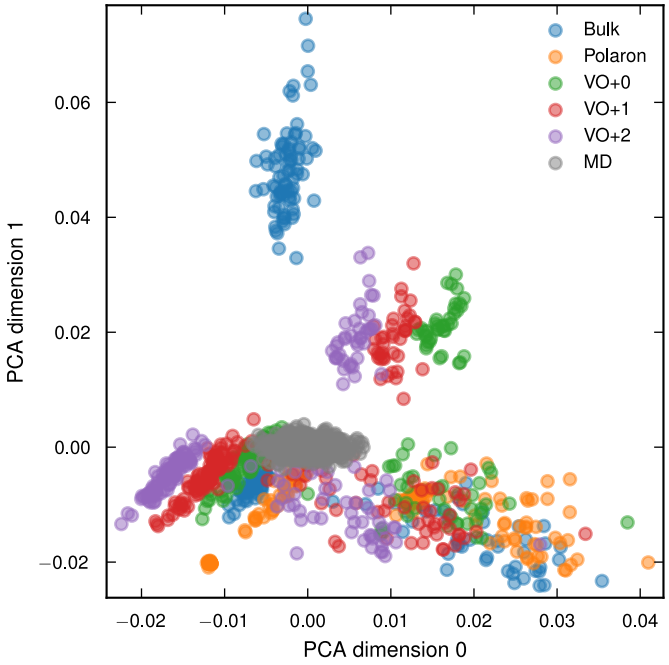

FIG. S2. Summary of the data acquisition workflow.

* ethan.berger@chalmers.se
† julia.wiktor@chalmers.se

II. TRAINING OF THE NEUROEVOLUTION POTENTIAL

The NEP was trained using the GPUMD package. The radial and angular cutoffs were set to 6 and 4 Å, respectively, descriptors were described using $n_{\max} = (8, 6)$ and $l_{\max} = (4, 0)$, the hidden layer contained 40 neurons, and the model was trained for 200×10^3 generations. The empirical short-ranged Ziegler-Biersack-Littmark (ZBL) potential was added using a cutoff of 1.5 Å [1]. Loss functions and parity plots for the resulting model are presented in Fig. S3.

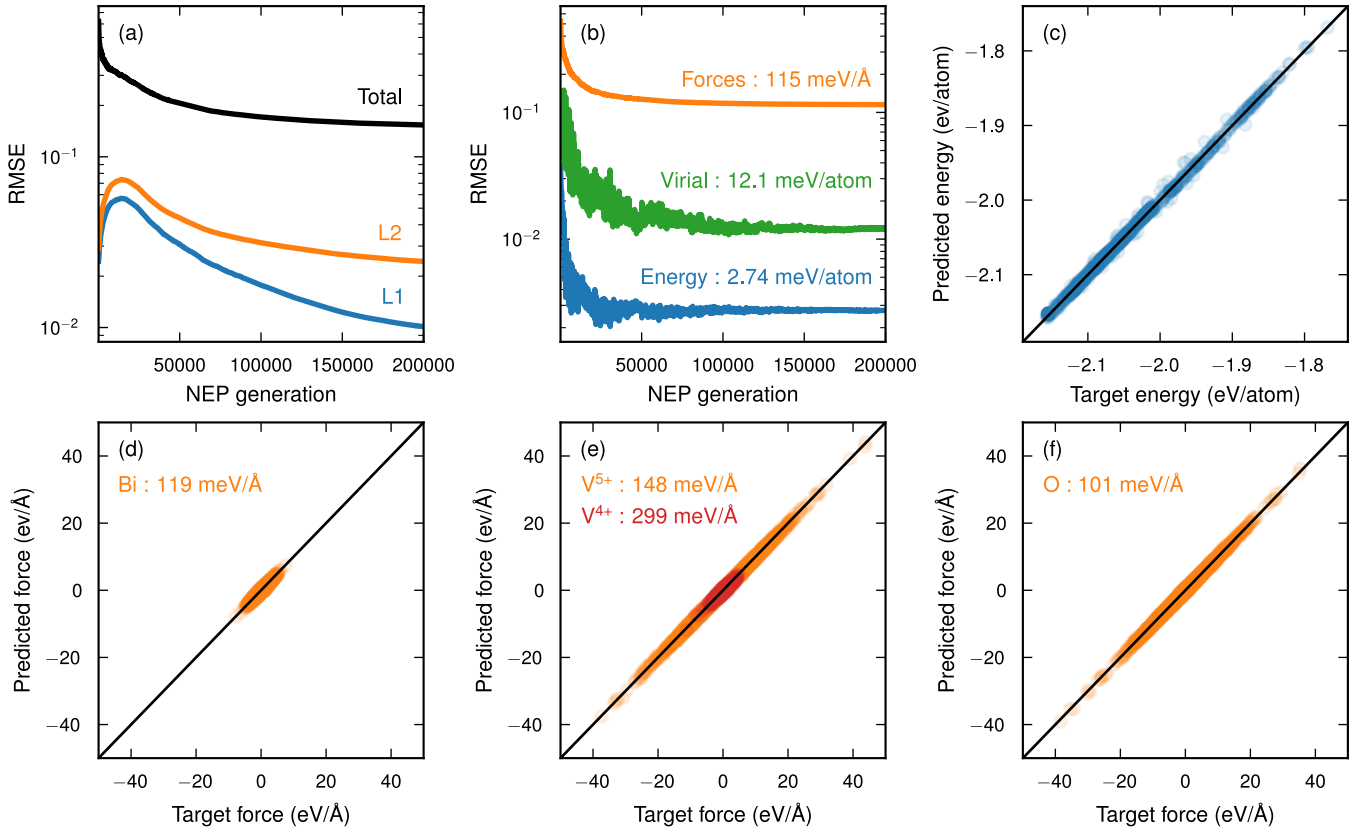

FIG. S3. (a) Total loss function and regularizatioin parameters L1 and L2 during training. (b) RMSE of the energy, force and virial during training. RMSEs of the final model are given. (c) Comparison between the target and predicted energy of the final model. (d-f) Comparison between target and predicted forces for each element. For vanadium, both V^{5+} and V^{4+} are shown in (e).

III. CONVERGENCE OF THE FREE ENERGY DIFFERENCE WITH SIMULATION LENGTH AND SUPERCELL SIZE

The convergence of free energy differences depends greatly on the length of the thermodynamic integration. Fig. S4 shows the free energy as a function of the simulation length at low and high temperatures. Both forward (H_i to H_f) and backward (H_f to H_i) are shown, alongside their mean. Since it is clear that the latter converges much faster, we find that the mean between 10^5 steps forward and backward is a good compromise between accuracy and computational effort, and therefore use this simulation length to produce all results.

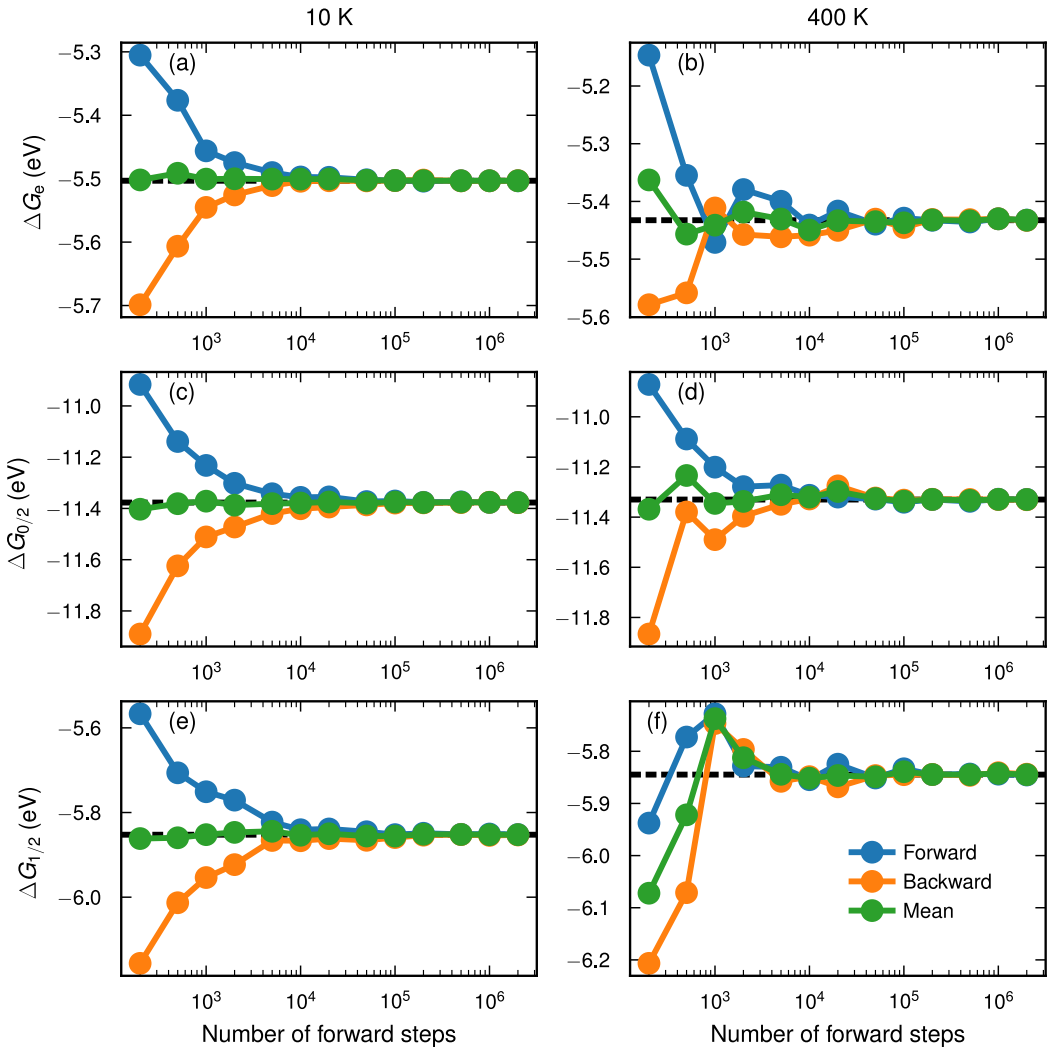

FIG. S4. Convergence of the free energy differences with the number of thermodynamic integration steps at 10 K (left panels) and 400 K (right panels).

Fig. S5 shows the convergence of the polaron free energy with the number of atoms in the supercell. While the free energy converges for supercells of ∼1000 atoms, we use $8\sqrt{2} \times 8\sqrt{2} \times 2$ supercells containing 12288 atoms to minimize finite-size effect, which remains a manageable number of atoms for NEP simulations.

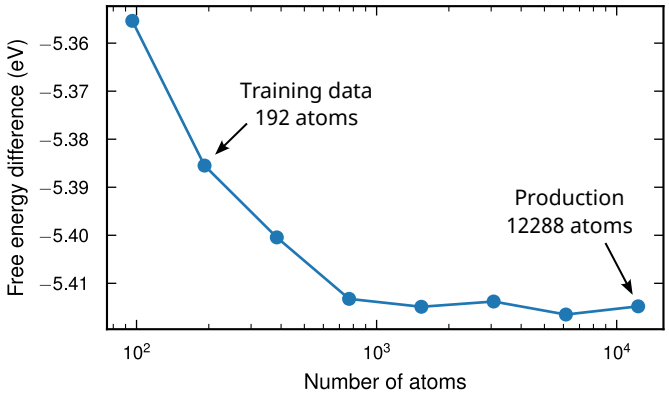

FIG. S5. Convergence of the free energy differences with the number of atoms. The supercell size used for training and production are highlighted with arrows.

IV. TEMPERATURE DEPENDENCE OF THE VERTICAL TRANSITIONS

Fig. S6 presents results for vertical transitions of a polaron and an oxygen defect. The left panels show, the center panels show the distribution of vertical transitions at low and high temperature, and the right panels show the transitions with temperature. Similar to the free energy presented in the main text, vertical transitions are found to be constant with temperature, which can again be explained by the high harmonicity of the PES. Although the transitions of the corner sharing VO_4 are constant with temperature [panel (i)], its PES does not look harmonic in panel (g). This could potentially be explained by a wrong choice of path between V^{5+} and V^{4+} when plotting the PES. All paths in Figs. S6 and Fig. 2 of the main text are obtained through linear interpolation between V^{5+} and V^{4+}.

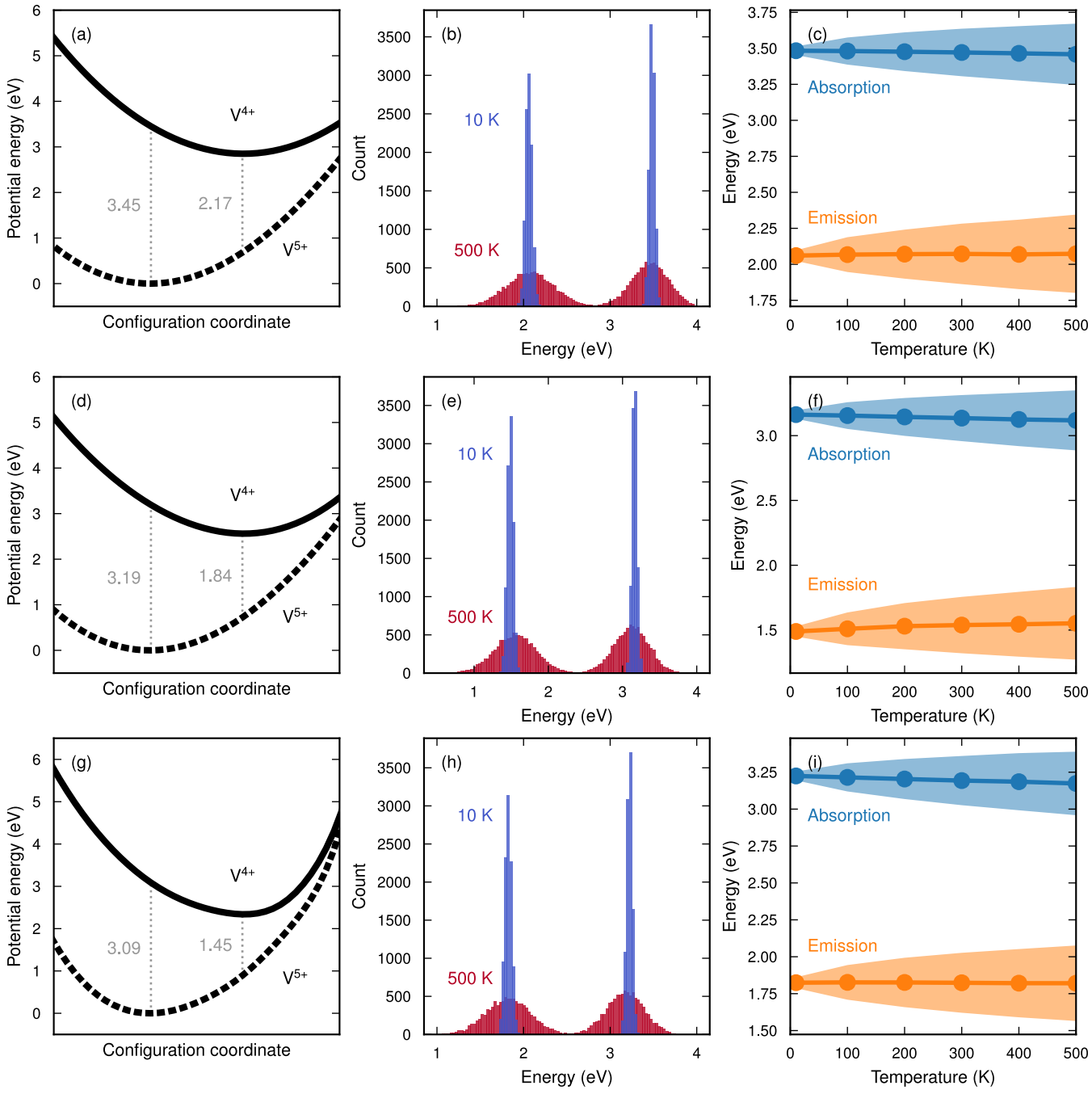

FIG. S6. (a) Potential energy surfaces of the pristine system and the electron polaron, for both V^{5+} and V^{4+}. (b) Histograms of both vertical transition energies at 100 K and 500 K. (c) Average emission and absorption vertical transition energies with temperature. (d-f) and (g-i) are the same as (a-c) for an electron localizing in the VO_3 and VO_4 corner sharing of an oxygen defect, respectively.

V. THERMAL EXPANSION

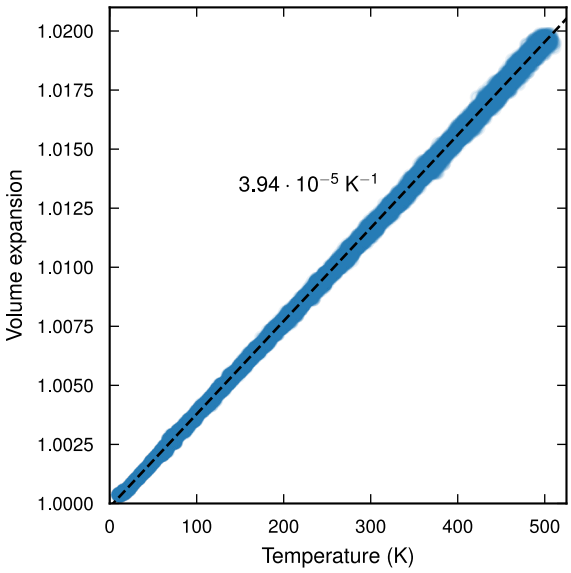

FIG. S7. Thermal expansion of bulk $BiVO_4$. The dashed black line shows a linear fit.

VI. EFFECT OF STRAIN ON THE POTENTIAL ENERGY SURFACE

Fig. S10 shows the impact of strain on the PES. It is clear that strain modifies the bond length of both V^{5+} and V^{4+}, which can also be seen from the RDF in Fig. 2(e). Additionally, tensile strain (in red) clearly decreases the transition energy between V^{5+} and V^{4+}, which in turn explains the shift of the CTL in Fig. 2(b) of the main text.

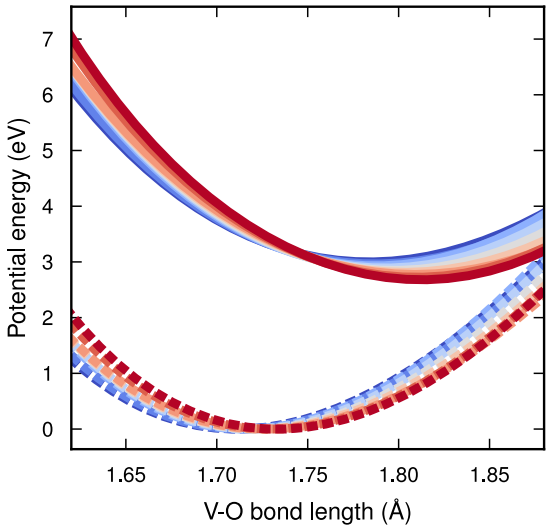

FIG. S8. PES at various strain between -2.0% and +2.0%. Compressive strain is in blue, and tensile in red. Solid and dashed lines correspond to V^{5+} and V^{4+}, respectively.

VII. CONFIGURATIONAL SAMPLING OF OXYGEN-VACANCY CHARGE STATES

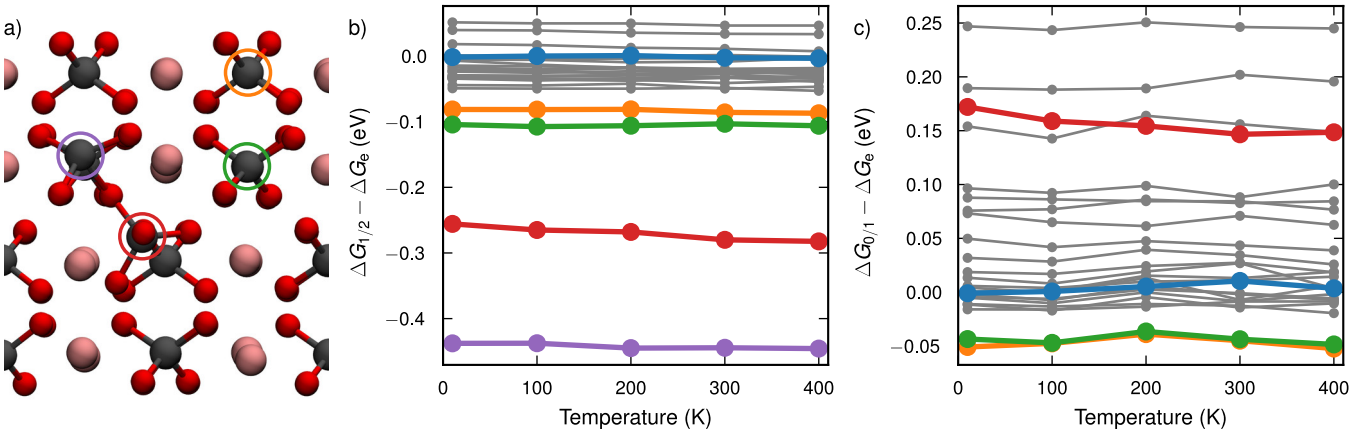

FIG. S9. (a) Atomistic structure of oxygen vacancy in $BiVO_4$, with vanadium sites at which electrons can localize highlighted by colored circles. (b–c) Free energy differences $\Delta G_{+1/+2}$ and $\Delta G_{0/+1}$ at various temperatures. Highlighted sites in panel (a) are shown in color, while gray lines show the other sites within 10 Å around the vacancy. Note that the free energies are shifted by the polaron free energy difference (ΔG_e) for comparison. In (b) and (c), the blue lines correspond to the free energy difference of a localized electron far away from the oxygen vacancy.

VIII. DIFFERENCE BETWEEN NPT AND NVT EQUILIBRATION

All results presented in the main text are obtained through thermodynamic integration after NPT equilibration. In Fig. S8, we present the movement of CTL with temperature for NVT equilibration. All absolute CTLs are found to slightly increased at high temperature, in contrast with the constant behavior observed for NPT equilibration. In practice, fixing the lattice constant results in compressive strain at high temperature. The increase observed in Fig. S8(b) and (d) can therefore be related to the one observed in Fig. 2(b) of the main text when applying compressive strain.

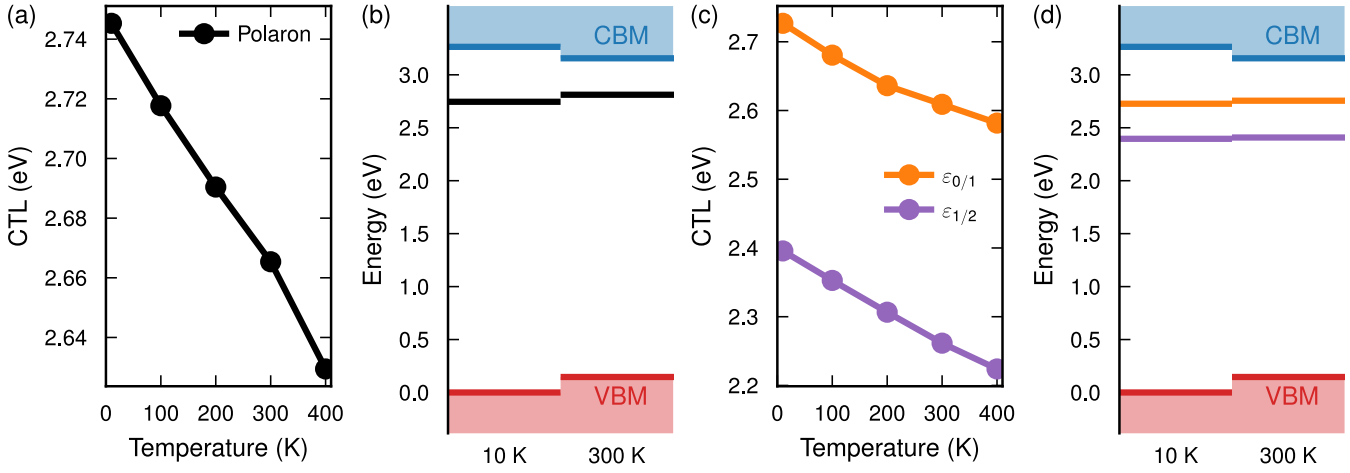

FIG. S10. Relative and absolute CTL from thermodynamic integration after NVT equilibration. (a) CTL of the polaron relative to the VBM. (b) Absolute CTL of the polaron within the band gap. (c) CTLs of the oxygen vacancy relative to the VBM. (d) Absolute CTLs of the oxygen vacancy within the band gap.

[1] Z. Yan, Z. Fan, and Y. Zhu, Improving robustness and training efficiency of machine-learned potentials by incorporating short-range empirical potentials, Journal of Chemical Information and Modeling **66**, 1406 (2026).